

Confinement-engineered superconductor to correlated-insulator transition in a van der Waals monolayer

Somesh Chandra Ganguli,^{*} Viliam Vaňo, Shawulienu Kezilebieke, Jose L. Lado,^{*}
and Peter Liljeroth^{*}

Department of Applied Physics, Aalto University, FI-00076 Aalto, Finland

E-mail: somesh.ganguli@aalto.fi; jose.lado@aalto.fi; peter.liljeroth@aalto.fi

Abstract

Transition metal dichalcogenides (TMDC) are a rich family of two-dimensional materials displaying a multitude of different quantum ground states. In particular, d^3 TMDCs are paradigmatic materials hosting a variety of symmetry broken states, including charge density waves, superconductivity, and magnetism. Among this family, NbSe₂ is one of the best-studied superconducting materials down to the monolayer limit. Despite its superconducting nature, a variety of results point towards strong electronic repulsions in NbSe₂. Here, we control the strength of the interactions experimentally via quantum confinement and use low-temperature scanning tunneling microscopy (STM) and spectroscopy (STS) to demonstrate that NbSe₂ is in close proximity to a correlated insulating state. This reveals the coexistence of competing interactions in NbSe₂, creating a transition from a superconducting to an insulating quantum correlated state by confinement-controlled interactions. Our results demonstrate the dramatic role of interactions in NbSe₂, establishing NbSe₂ as a correlated superconductor with competing interactions.

Niobium dichalcogenides, and in particular NbSe₂ is well-known to be a paradigmatic superconducting two-dimensional material and it realizes Ising superconductivity at the monolayer (ML) limit.¹⁻³ Due to its superconducting nature, NbSe₂ has been considered to be a metal where Coulomb repulsions play a marginal role and the superconducting state arises from conventional electron-phonon coupling.⁴ Indeed, the emergence of charge density wave states is usually attributed to soft-phonon modes,⁵⁻¹⁰ so that symmetry broken states are not related with strong Coulomb interactions.

Despite the apparent marginal role of the Coulomb repulsion in NbSe₂, related compounds in the dichalcogenide family show strong correlations.¹¹⁻¹⁵ In particular, VSe₂ is known to be a strongly correlated material,¹⁶ with competing correlated states including a potential magnetic Mott insulating state.^{14,17-19} The chemical similarity between NbSe₂ and VSe₂, contrasted with their dramatically different electronic properties, motivates the question of whether NbSe₂ exhibits a strongly correlated superconducting state, in contrast with the originally assumed weakly interacting scenario.²⁰⁻²³ In that regard, theoretical calculations have shown that NbSe₂ is close to a Mott insulating transition to a ferromagnetic state.²⁰⁻²³ These results suggest that competing interactions coexist in NbSe₂ system, and in particular suggest the possibility of the superconducting state coexisting with strong Coulomb interactions.

In this manuscript, we experimentally demonstrate that ML NbSe₂ is in proximity to a correlated insulating state, by controlling the strength of the electronic interactions by quantum confinement effects. In particular, we show that for ML NbSe₂ islands of size several times the coherence length, repulsive electronic interactions create a phase transition from a superconducting to a correlated insulating state. This behavior is rationalized from a competing interaction scenario (Fig. 1(a)), in which attractive electron-phonon interactions compete with strongly repulsive Coulomb interactions. The electron-phonon interactions that give rise to a superconducting ground state do not depend on the system size, and will dominate if the system size is increased sufficiently (Fig. 1(b)). On the other hand, the

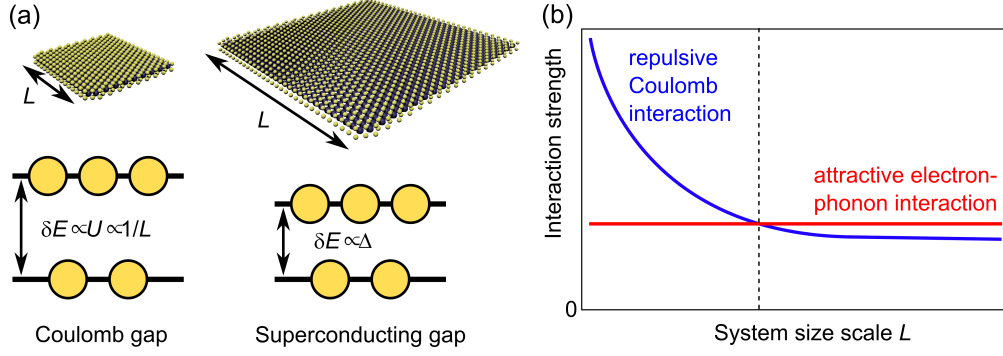


Figure 1: (a) Sketches of small and large NbSe₂ islands with the associated Coulomb or superconducting gaps. (b) Schematic dependence of the attractive and repulsive interactions on the system size.

repulsive Coulomb interactions are strongly dependent on the system size ($U \propto 1/L^{24-26}$) and will drive the system into Coulomb-gapped, correlated state as the system size is decreased. This picture is complementary to the classical interpretation in terms of Coulomb blockade, and completely analogous to the approach taken in, e.g., interpreting the correlated insulating states in twisted bilayer graphene in terms of local repulsion.²⁶ We test this behaviour experimentally by tuning the size of NbSe₂ islands and using low-temperature scanning tunneling microscopy (STM) and spectroscopy (STS) to measure the type and magnitude of the resulting energy gap. Our results provide a quantitative experimental bound on the strength of repulsive interactions of NbSe₂, highlighting a non-trivial impact of correlations in superconducting dichalcogenides.

Experimental superconducting-correlated transition. We grow NbSe₂ (Fig. 2(a)) on a highly-oriented pyrolytic graphite (HOPG) substrate with a sub-monolayer coverage. By adjusting the growth conditions (see Supporting Information (SI) for details), we achieve a sample with a wide variety of island sizes and their relative separations. This creates an ideal platform to study the effects of quantum-confinement enhanced correlations. The island sizes vary between a few hundreds of nm² to several tens of thousands of nm² (lateral sizes few tens of nm to several hundreds of nm, see SI for island size determination). Fig. 2(b) shows an STM image of a representative area (500×500 nm²), where this size variation of

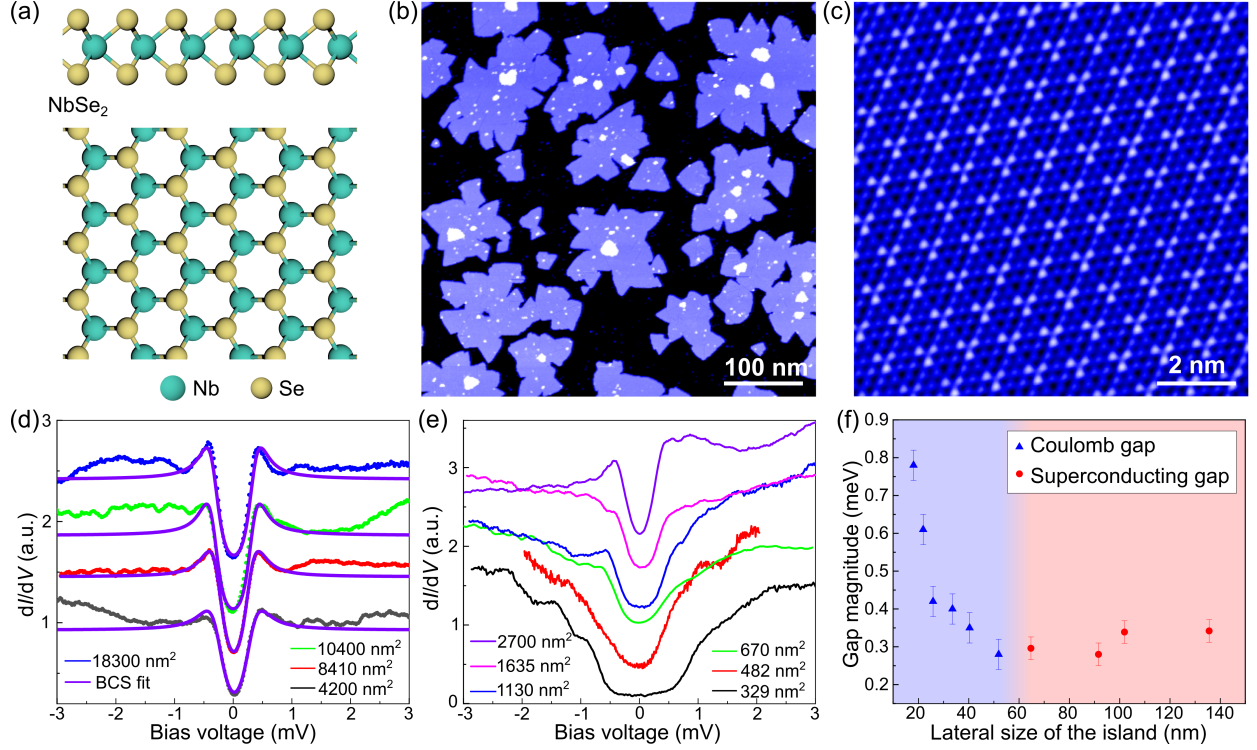


Figure 2: (a) Side and top view schematics of monolayer NbSe₂. (b) Large-scale STM image of monolayer NbSe₂ on HOPG showing a large variation of island sizes. (c) Atomic resolution image of monolayer NbSe₂ showing 3×3 charge density wave modulation. (d, e) Variation of the superconducting (d) and Coulomb (e) gap with island size. Spectra have been normalized and offset vertically. Superconducting gaps in panel (d) have been fit with the Dynes equation (solid purple lines). (f) Evolution of the gap magnitude extracted from the tunneling spectra as a function of the island size showing a transition from Coulomb gap-like to superconducting spectra as the size is increased. The shape of the measured spectrum is indicated by the different symbols: blue triangles and red circles for the spectra exhibiting Coulomb- and SC-type gaps, respectively.

individual ML islands is apparent. Each individual island has atomically sharp edges and show the well-known 3×3 charge density wave (CDW) modulation similar to extended ML NbSe₂ (Fig. 2(c)). While the data shown in Fig. 2(c) was acquired on a NbSe₂ island with a lateral size of ~ 92 nm (area 8400 nm²), the CDW modulation persists down to islands sizes of < 500 nm² (see SI). We characterize the electronic properties of each individual island by carrying out spatially resolved tunneling conductance (dI/dV) measurement (see Methods section for details). Typical examples of the dI/dV spectra are shown in Figs. 2(d) and 2(e). The spectra can be divided into two groups based on qualitative differences. Islands with

sizes 4200 nm^2 and above show density of states consistent with BCS-like behaviour with particle-hole symmetric coherence peaks (Fig. 2(d)), which indicate a presence of phase-coherent Cooper pairs. On the other hand, islands with sizes 2700 nm^2 and below have distinctive particle-hole asymmetric density of states (Figure 2(e)) with no coherence peaks. This transition occurs at a size range several times larger than the coherence length of NbSe₂ ($\sim 7 \text{ nm}$, see below).

Such asymmetric differential conductance is typical of inelastic steps associated to correlated Coulomb excitations.²⁷⁻²⁹ Furthermore, the magnitude of the energy gap in these islands monotonically increases with decreasing island size (Fig. 2(f), the details of extracting the energy gap are given in the SI).^{24,30} This behaviour is consistent with the presence of a Coulomb gap in small islands, where the repulsive Coulomb interaction dominates over phonon-mediated attractive interactions. On the other hand, the BCS-shaped superconducting gaps in the islands in Fig. 2(d) are independent of the island size (Fig. 2(f)) as the electron-phonon coupling strength does not depend on the system size. The Coulomb gap and superconducting gaps can also be distinguished by their respective magnetic field dependent behaviour (see SI).

Disorder driven superconductor-insulator transition (SIT) cannot justify our data, since we observe that the SC gap remains practically constant with reducing island size. The data also suggests that disorder does not have a sizable impact besides a small renormalization of the density of states as given by the Altshuler-Aronov effect.^{31,32} The main source of disorder appears to be on the edges of the islands which show slightly different SC energy gap compared to the center of the island (see SI).

Theoretical model for competing interactions. However, the previous phenomenology can be rationalized with a many-body low energy model. Many-body interactions are well known to lead to Coulomb blockade effects in conventional superconductors, promoting intriguing phenomena arising from the interplay of pairing correlations and finite size effects.^{33,34} However, these phenomena has remained unexploited to probe many-body effects

in correlated two-dimensional superconductors. Since the full quantum many-body system for a nm-sized island cannot be exactly solved, we will focus on the instability of the lowest energy $2n$ single-particle eigenstates of the NbSe₂ island $\Psi_{i,s}$, with $i = 1, \dots, n$ the state number and $s = \uparrow, \downarrow$ the spin quantum number. These states closest to the Fermi energy will be the ones most impacted by interactions, and therefore the fundamental physics of the system can be captured by projecting electronic interactions in this manifold. For the sake of concreteness, we take interactions $SU(2)$ symmetric and constant on the Fermi surface manifold. In particular, we take projected electronic interactions partitioned into intra-orbital repulsive ones U (of Coulomb origin) and inter-orbital attractive ones V (of electron-phonon origin). Furthermore, due to the existence of nearby large superconducting islands, the low energy states will feel a superconducting proximity effect with a value depending on the distance to the closest big superconducting island. We parametrize this effect with $\bar{\Delta}$. The half filling of the low energy manifold is enforced by μ , and computed self-consistently for each U and V . The low energy many-body Hamiltonian takes the form.

$$\begin{aligned}
\mathcal{H} = & \sum_i U \Psi_{i,\uparrow}^\dagger \Psi_{i,\uparrow} \Psi_{i,\downarrow}^\dagger \Psi_{i,\downarrow} \\
& - \sum_{i,j>i,s,s'} V \Psi_{i,s}^\dagger \Psi_{i,s} \Psi_{j,s'}^\dagger \Psi_{j,s'} \\
& + \mu \sum_{i,s} \Psi_{i,s}^\dagger \Psi_{i,s} + \bar{\Delta} \sum_i \Psi_{i,\uparrow}^\dagger \Psi_{i,\downarrow}^\dagger + \text{H.c.}
\end{aligned} \tag{1}$$

The projected electron-phonon interaction V is taken to be independent on the system size, whereas the projected Coulomb repulsive interaction U will get enhanced as the system size L becomes smaller as $U = U_0 + \frac{e_0}{L}$ due to the long-range tail of Coulomb interactions. The effective model is solved using exact diagonalization, projecting the electronic repulsion onto the lowest energy states, and solving the projected Hamiltonian exactly. This is, of course, an approximate procedure when a finite number of states is considered, and we verified that our results are not qualitatively modified when including a higher number of

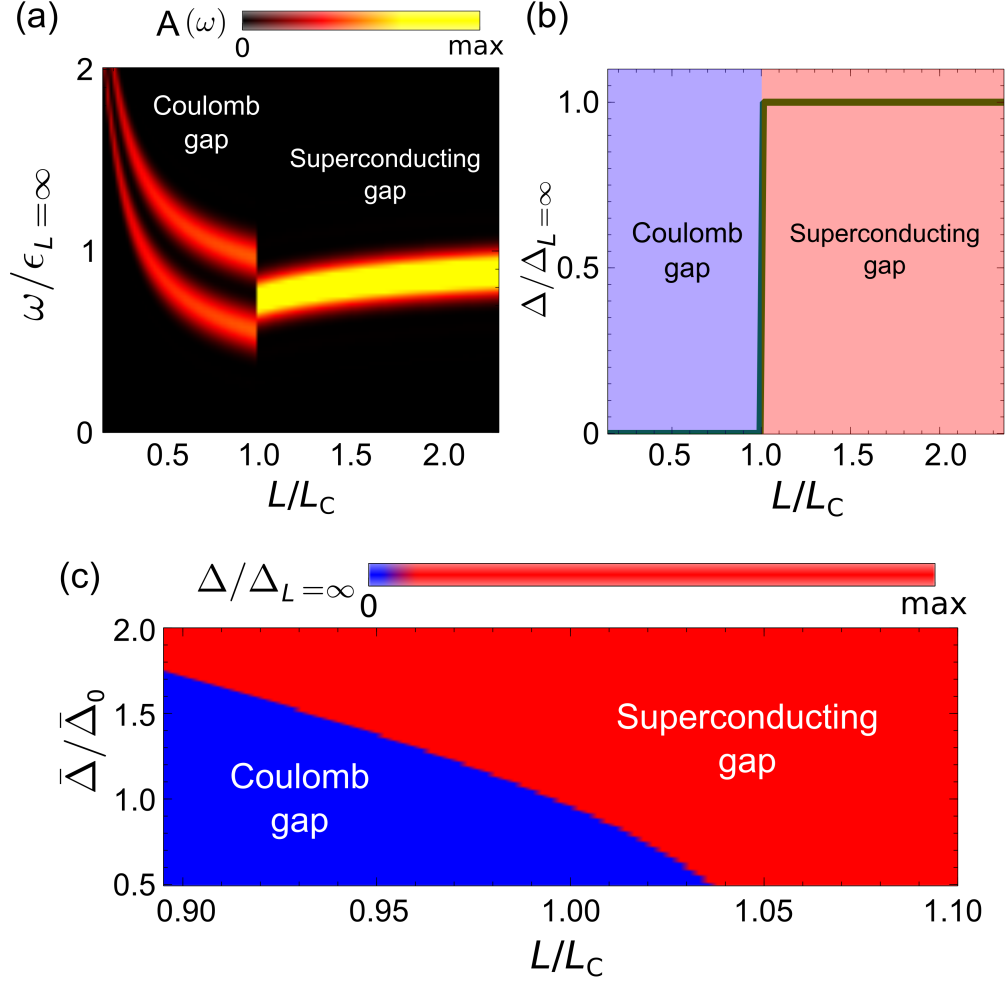


Figure 3: (a,b,c) Electron spectral function as a function of the system size (a), and induced superconductivity as a function of the system size (b). It is shown that a transition between the superconducting and the correlated state takes place without gap closing. For correlated islands close to the phase transition, increasing the superconducting proximity effect $\bar{\Delta}$ can push the system to the superconducting region as shown in panel (c). We took $2n = 8$ for A-C, $U_0 = 2$ V and L_C is the critical length for $\bar{\Delta}_0 = 0.4$ V.

orbitals. For such a many-body Hamiltonian the single-electron density of states can be computed as $A(\omega) = \sum_{i,s} \langle \Omega | \Psi_{i,s} \delta(\omega - \mathcal{H} + E_0) \Psi_{i,s}^\dagger | \Omega \rangle$, where E_0 is the many-body energy and $|\Omega\rangle$ the many-body ground state.

We show in Fig. 3(a) the single-electron spectral function $A(\omega)$ as a function of the system size L , where the transition between a Coulomb dominated gap ϵ_L to a superconducting dominated one can be seen. For large system size $L \rightarrow \infty$, the system shows a superconducting gap stemming from the attractive interactions and pinned by the superconducting

proximity $\bar{\Delta}$. It is worth noting that, as the system is finite, observing a sharp phase transition from zero to finite superconducting order requires a finite value of the proximity effect $\bar{\Delta}$. Once the system size goes below a critical value L_C , the nature of the excitation gap ϵ_L changes, yet without a gap closing. The different nature of the two gaps above and below the transition point $L = L_C$ can be verified by computing the superconducting expectation value $\Delta = \sum_i \langle \Psi_{i,\uparrow} \Psi_{i,\downarrow} \rangle$, showing that associated with the discontinuous jump as the size becomes smaller, the superconducting order parameter suddenly disappears (Fig. 3(b)). We note that for small islands the observed spectra featuring a continuum of states above the gap are fundamentally different from the ones expected for systems with confined energy levels. The transition between the correlated gap for small islands and superconducting one for large islands is found to be of first order, with a discontinuity on the gap. This is consistent with our experimental data and therefore strongly supports the competing interaction scenario.

Due to the proximity of NbSe₂ to the phase transition point, it is expected that an external perturbation can cause a critical system to drift to different regions of the phase diagram. In particular, increasing a superconducting proximity effect $\bar{\Delta}$ would push the system toward the superconducting gapped region. This can be verified as shown in Fig. 3(c) where it can be seen that ramping up the superconducting proximity pushes the system that originally has a correlated gap towards a superconducting gap. While this is shown for reduced range in Fig. 3(c), the very same mechanism applies in a broader range of L and Δ . We have verified that the same behavior remains qualitatively unchanged upon increasing the number of orbitals considered in the many-body Hamiltonian (shown in the SI).

It is well-known that 2H-NbSe₂ exhibits charge-density wave order at low temperatures and the presence of Ising-type spin-orbit coupling might also have an effect on the observed behaviour.^{2,4,7,8,35} However, by using a more detailed model incorporating these two effects (see SI), we can demonstrate that the observed phenomenology is a genuine Coulomb effect. Ising spin-orbit coupling leads to momentum dependent spin splitting in the Brillouin zone.

As this perturbation respects time-reversal symmetry, it does not have a detrimental impact on spin-singlet superconducting state. Ising SOC will also not impact the Coulomb electronic interactions, as the momentum-dependent exchange splitting does not change the underlying atomic nature of the orbitals, which is the one that ultimately determines the strength of the local and non-local interactions.

The NbSe₂ charge density wave gives rise to band folding and splitting, yet maintaining the system metallic. Even though the low energy states now become modulated in space following the CDW profile, the repulsive Coulomb interactions are not qualitatively affected. This is rationalized from the fact that electronic repulsion is an atomic property associated to the Wannier states, and thus again independent on larger scale structural reconstructions. The CDW also does not substantially impact the mechanism for superconductivity, since such reconstruction does not break time-reversal symmetry, the relevant symmetry that could strongly impact the spin-singlet superconducting state.

Proximity induced quantum phase transition. Based on the previous results, we check this proximity-induced phase transition experimentally by comparing the spectra of different critical islands with different respective distances to a big superconducting island, probing whether the superconducting proximity effect transforms the correlated gap into a superconducting one. We start by quantifying the proximity effect in the NbSe₂/HOPG-system as shown in Figs. 4(a-c). Measuring dI/dV spectra close to a SC NbSe₂ shows a proximity-induced gap on HOPG and tracking the spatial evolution allows us to estimate the decay length. Fitting the spatially dependent dI/dV in Fig. 4(b) to Dynes equation, we extract the gap as a function of the distance from the NbSe₂ island edge (Fig. 4(c)). An exponential fitting of Dynes gap with distance yields $\xi \approx 7$ nm (see SI).

We then proceed to show the effect of proximity in the non-superconducting islands showing size-dependent Coulomb gaps. We selected 2 representative island sizes of 330 nm² and 650 nm² (Fig. 4(d,e), additional results on spatially resolved spectroscopy are shown in the SI). Here, the smaller of the islands is well into the Coulomb gapped regime, but the

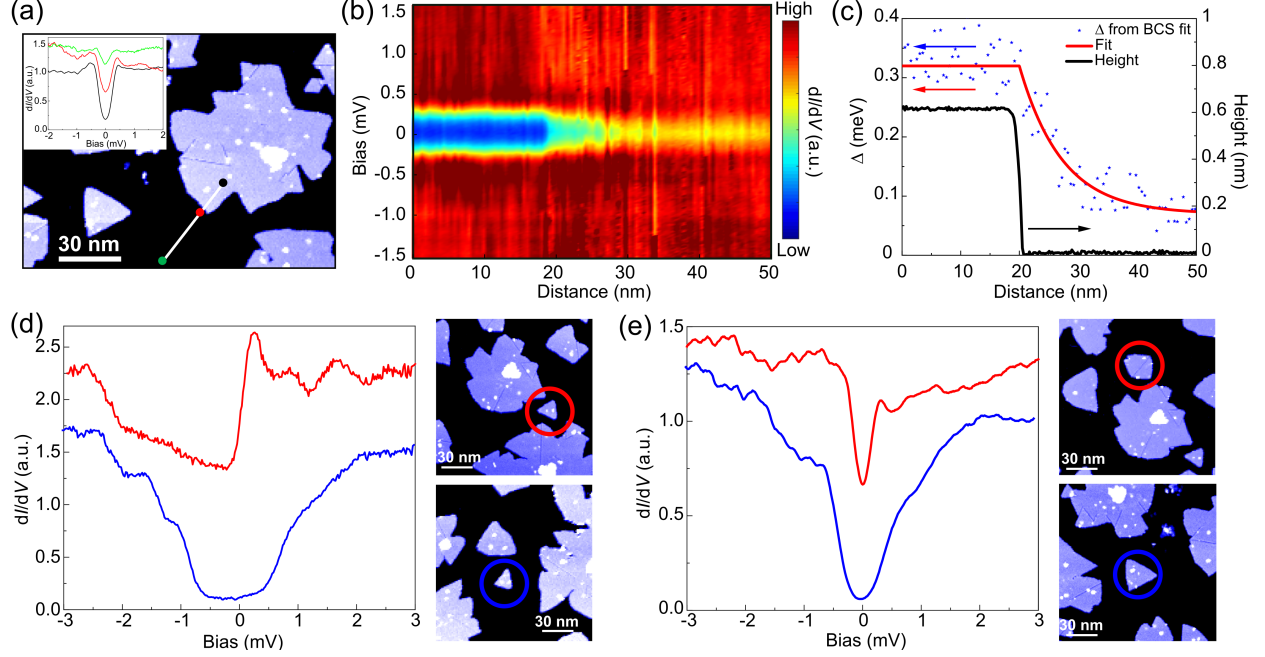


Figure 4: (a) STM image showing NbSe₂ monolayer island. dI/dV spectra measured in black, green and red points are shown in the inset with corresponding colors. (b) dI/dV spectra measured along the white line in panel (a) presented as a color scale plot. Black (green) point in (a) is the left (right) edge of (b). (c) Fitted SC gap, its exponential fit along with the height profile measured along the white line in panel (a). (d,e) Proximity induced superconductivity in Coulomb gapped islands. dI/dV spectra and topographic images of (d) an isolated island of size 330 nm² (blue circle) and an island of size 330 nm² in proximity with larger SC island (red circle), and (e) an isolated island of size 650 nm² (blue circle) and an island of size 650 nm² in proximity with larger SC island (red circle). Scale bars, 30 nm. Spectra in panels (d) and (e) are offset vertically for clarity.

larger one is closer to phase transition determined in Fig. 2(f). When each of these islands are not in proximity (~ 7 nm) to any superconducting islands (Figs. 4(d,e)), they show particle-hole asymmetric Coulomb gap (Figs. 4(d,e), blue lines). Island with size 650 nm² in proximity to a larger superconducting island shows a drastically different conductance with gap value comparable to the BCS gap observed in larger islands (Fig. 4(e), red line), indicating that the proximity effect is sufficient to push the system into the superconducting phase. Strong particle-hole asymmetric feature indicates significant presence of correlation in this proximity-induced superconducting island. The magnetic field dependent behaviour of proximitized island is also indicative of the presence of superconducting order (see SI). On the other hand, island with size 330 nm² in proximity to a larger superconducting island

shows a complex spectra with no clear gap signature (Fig. 4(d), red line), indicating that the proximity-induced Josephson coupling is not sufficient to overcome Coulomb repulsion to induce superconducting order in this island.

Conclusions. We have demonstrated that ML NbSe₂ can be pushed to a correlated regime, driving a quantum phase transition from superconducting to a correlated gap. This transition is rationalized from the existence of competing interactions, in which the coexistence of attractive electron-phonon interactions, driving superconductivity, and repulsive Coulomb interactions, driving correlated insulating behavior, allows to dramatically change the nature of the ground state in NbSe₂ by slightly enhancing the Coulomb interactions. The Coulomb gap observed in our system is inherently different from the single-particle gap observed in small metallic islands.³⁶ The dI/dV spectra in the smallest NbSe₂ islands (Fig. 2(e)) show a continuum of states above the gap rather than a discrete set of states,³⁷ indicating many-body nature of the gap in our system. While it is possible to analyze our data using the Coulomb blockade model typically employed for 3D superconductors,^{38–40} it is worthwhile to note that these systems are weakly interacting being far from any Stoner instability and electron induced symmetry breaking, whereas NbSe₂ is in close proximity to correlated state which can be driven by perturbations such as strain.²³ Also, the SIT mechanism observed here veers away from the traditional disorder-driven scenario. In comparison, similar SIT has been observed by controlling electronic interactions in twisted van der Waals multilayers.⁴¹

The critical role of Coulomb interactions highlighted in our results suggests a potentially crucial impact of electronic correlations for the emergence of both charge density wave orders and superconductivity besides the typical electron-phonon driven scenarios. Recent results show the presence of spin-fluctuations in ML NbSe₂⁴² and nematic superconductivity in few layer NbSe₂,⁴³ which are indicative of its proximity to correlated regime. We finally showed that for correlated NbSe₂ samples close to the phase transition, superconducting proximity effect strongly impacts the ground state, pushing the system through the superconductor-

correlated phase boundary. Ultimately, these results suggest that due to the close to critical behavior of NbSe₂, correlated states could be promoted in NbSe₂ by screening,⁴¹ chemical⁴⁴ or twist engineering,⁴⁵ putting forward d^3 chalcogenides as paradigmatic strongly correlated two-dimensional materials.

Supporting Information Available

Experimental methods, and additional experimental and theoretical results.

Acknowledgement

This research made use of the Aalto Nanomicroscopy Center (Aalto NMC) facilities and was supported by the European Research Council (ERC-2017-AdG no. 788185 “Artificial Designer Materials”) and Academy of Finland (Academy professor funding nos. 318995 and 320555, Academy postdoctoral researcher no. 309975, Academy research fellow nos. 331342 and 336243). We acknowledge the computational resources provided by the Aalto Science-IT project. We thank Xin Huang and Héctor González-Herrero for their help with the temperature dependence of the NbSe₂ growth.

References

- (1) Ugeda, M. M.; Bradley, A. J.; Zhang, Y.; Onishi, S.; Chen, Y.; Ruan, W.; Ojeda-Aristizabal, C.; Ryu, H.; Edmonds, M. T.; Tsai, H.-Z.; Riss, A.; Mo, S.-K.; Lee, D.; Zettl, A.; Hussain, Z.; Shen, Z.-X.; Crommie, M. F. Characterization of Collective Ground States in Single-Layer NbSe₂. *Nat. Phys.* **2016**, *12*, 92–97.
- (2) Xi, X.; Wang, Z.; Zhao, W.; Park, J.-H.; Law, K. T.; Berger, H.; Forró, L.; Shan, J.; Mak, K. F. Ising pairing in superconducting NbSe₂ atomic layers. *Nat. Phys.* **2016**, *12*, 139–143.

- (3) Zhao, K.; Lin, H.; Xiao, X.; Huang, W.; Yao, W.; Yan, M.; Xing, Y.; Zhang, Q.; Li, Z.-X.; Hoshino, S.; Wang, J.; Zhou, S.; Gu, L.; Bahramy, M. S.; Yao, H.; Nagaosa, N.; Xue, Q.-K.; Law, K. T.; Chen, X.; Ji, S.-H. Disorder-induced multifractal superconductivity in monolayer niobium dichalcogenides. *Nat. Phys.* **2019**, *15*, 904–910.
- (4) Valla, T.; Fedorov, A. V.; Johnson, P. D.; Glans, P.-A.; McGuinness, C.; Smith, K. E.; Andrei, E. Y.; Berger, H. Quasiparticle Spectra, Charge-Density Waves, Superconductivity, and Electron-Phonon Coupling in 2H-NbSe₂. *Phys. Rev. Lett.* **2004**, *92*, 086401.
- (5) Soumyanarayanan, A.; Yee, M. M.; He, Y.; van Wezel, J.; Rahn, D. J.; Rossnagel, K.; Hudson, E. W.; Norman, M. R.; Hoffman, J. E. Quantum phase transition from triangular to stripe charge order in NbSe₂. *Proc. Nat. Acad. Sci.* **2013**, *110*, 1623–1627.
- (6) Lian, C.-S.; Si, C.; Duan, W. Unveiling Charge-Density Wave, Superconductivity, and Their Competitive Nature in Two-Dimensional NbSe₂. *Nano Lett.* **2018**, *18*, 2924–2929.
- (7) Bianco, R.; Monacelli, L.; Calandra, M.; Mauri, F.; Errea, I. Weak Dimensionality Dependence and Dominant Role of Ionic Fluctuations in the Charge-Density-Wave Transition of NbSe₂. *Phys. Rev. Lett.* **2020**, *125*, 106101.
- (8) Xi, X.; Zhao, L.; Wang, Z.; Berger, H.; Forró, L.; Shan, J.; Mak, K. F. Strongly enhanced charge-density-wave order in monolayer NbSe₂. *Nat. Nanotechnol.* **2015**, *10*, 765–769.
- (9) Weber, F.; Rosenkranz, S.; Castellán, J.-P.; Osborn, R.; Hott, R.; Heid, R.; Bohnen, K.-P.; Egami, T.; Said, A. H.; Reznik, D. Extended Phonon Collapse and the Origin of the Charge-Density Wave in 2H-NbSe₂. *Phys. Rev. Lett.* **2011**, *107*, 107403.
- (10) Gye, G.; Oh, E.; Yeom, H. W. Topological Landscape of Competing Charge Density Waves in 2H-NbSe₂. *Phys. Rev. Lett.* **2019**, *122*, 016403.

- (11) O'Hara, D. J.; Zhu, T.; Trout, A. H.; Ahmed, A. S.; Luo, Y. K.; Lee, C. H.; Brenner, M. R.; Rajan, S.; Gupta, J. A.; McComb, D. W.; Kawakami, R. K. Room Temperature Intrinsic Ferromagnetism in Epitaxial Manganese Selenide Films in the Monolayer Limit. *Nano Lett.* **2018**, *18*, 3125–3131.
- (12) Manzeli, S.; Ovchinnikov, D.; Pasquier, D.; Yazyev, O. V.; Kis, A. 2D transition metal dichalcogenides. *Nat. Rev. Mater.* **2017**, *2*, 17033.
- (13) Wu, S.; Fatemi, V.; Gibson, Q. D.; Watanabe, K.; Taniguchi, T.; Cava, R. J.; Jarillo-Herrero, P. Observation of the quantum spin Hall effect up to 100 kelvin in a monolayer crystal. *Science* **2018**, *359*, 76–79.
- (14) Chen, P.; Pai, W. W.; Chan, Y.-H.; Madhavan, V.; Chou, M. Y.; Mo, S.-K.; Fedorov, A.-V.; Chiang, T.-C. Unique Gap Structure and Symmetry of the Charge Density Wave in Single-Layer VSe₂. *Phys. Rev. Lett.* **2018**, *121*, 196402.
- (15) Qiao, S.; Li, X.; Wang, N.; Ruan, W.; Ye, C.; Cai, P.; Hao, Z.; Yao, H.; Chen, X.; Wu, J.; Wang, Y.; Liu, Z. Mottness Collapse in 1T-TaS_{2-x}Se_x Transition-Metal Dichalcogenide: An Interplay between Localized and Itinerant Orbitals. *Phys. Rev. X* **2017**, *7*, 041054.
- (16) Duvjir, G.; Choi, B. K.; Jang, I.; Ulstrup, S.; Kang, S.; Ly, T. T.; Kim, S.; Choi, Y. H.; Jozwiak, C.; Bostwick, A.; Rotenberg, E.; Park, J.-G.; Sankar, R.; Kim, K.-S.; Kim, J.; Chang, Y. J. Emergence of a Metal–Insulator Transition and High-Temperature Charge-Density Waves in VSe₂ at the Monolayer Limit. *Nano Lett.* **2018**, *18*, 5432–5438.
- (17) Bonilla, M.; Kolekar, S.; Ma, Y.; Diaz, H. C.; Kalappattil, V.; Das, R.; Eggers, T.; Gutierrez, H. R.; Phan, M.-H.; Batzill, M. Strong room-temperature ferromagnetism in VSe₂ monolayers on van der Waals substrates. *Nat. Nanotechnol.* **2018**, *13*, 289–293.
- (18) Wong, P. K. J. et al. Evidence of Spin Frustration in a Vanadium Diselenide Monolayer Magnet. *Adv. Mater.* **2019**, *31*, 1901185.

- (19) Kezilebieke, S.; Huda, M. N.; Dreher, P.; Manninen, I.; Zhou, Y.; Sainio, J.; Mansell, R.; Ugeda, M. M.; van Dijken, S.; Komsa, H.-P.; Liljeroth, P. Electronic and magnetic characterization of epitaxial VSe₂ monolayers on superconducting NbSe₂. *Commun. Phys.* **2020**, *3*, 116.
- (20) Zhou, Y.; Wang, Z.; Yang, P.; Zu, X.; Yang, L.; Sun, X.; Gao, F. Tensile Strain Switched Ferromagnetism in Layered NbS₂ and NbSe₂. *ACS Nano* **2012**, *6*, 9727–9736.
- (21) Zheng, F.; Zhou, Z.; Liu, X.; Feng, J. First-principles study of charge and magnetic ordering in monolayer NbSe₂. *Phys. Rev. B* **2018**, *97*, 081101(R).
- (22) Divilov, S.; Wan, W.; Dreher, P.; Bölen, E.; Sánchez-Portal, D.; Ugeda, M. M.; Ynduráin, F. Magnetic correlations in single-layer NbSe₂. *J. Phys.: Condens. Matter* **2021**, *33*, 295804.
- (23) Wickramaratne, D.; Khmelevskiy, S.; Agterberg, D. F.; Mazin, I. I. Ising Superconductivity and Magnetism in NbSe₂. *Phys. Rev. X* **2020**, *10*, 041003.
- (24) Kouwenhoven, L. P.; Austing, D. G.; Tarucha, S. Few-electron quantum dots. *Rep. Prog. Phys.* **2001**, *64*, 701–736.
- (25) Guinea, F.; Walet, N. R. Electrostatic effects, band distortions, and superconductivity in twisted graphene bilayers. *Proc. Nat. Acad. Sci.* **2018**, *115*, 13174–13179.
- (26) Nuckolls, K. P.; Oh, M.; Wong, D.; Lian, B.; Watanabe, K.; Taniguchi, T.; Bernevig, B. A.; Yazdani, A. Strongly correlated Chern insulators in magic-angle twisted bilayer graphene. *Nature* **2020**, *588*, 610–615.
- (27) Heinrich, A. J.; Gupta, J. A.; Lutz, C. P.; Eigler, D. M. Single-Atom Spin-Flip Spectroscopy. *Science* **2004**, *306*, 466–469.

- (28) Khajetoorians, A. A.; Chilian, B.; Wiebe, J.; Schuwalow, S.; Lechermann, F.; Wiesendanger, R. Detecting excitation and magnetization of individual dopants in a semiconductor. *Nature* **2010**, *467*, 1084–1087.
- (29) Bryant, B.; Toskovic, R.; Ferrón, A.; Lado, J. L.; Spinelli, A.; Fernández-Rossier, J.; Otte, A. F. Controlled Complete Suppression of Single-Atom Inelastic Spin and Orbital Cotunneling. *Nano Lett.* **2015**, *15*, 6542–6546.
- (30) Ihn, T. *Semiconductor Nanostructures*; Oxford University Press: Oxford, 2009; pp 341–407.
- (31) Altshuler, B.; Aronov, A. In *Electron–Electron Interactions in Disordered Systems*; Efros, A., Pollak, M., Eds.; Elsevier: Amsterdam, 1985; pp 1–153.
- (32) Zhou, C.; Guo, H. Altshuler-Aronov effects in nonequilibrium disordered nanostructures. *Phys. Rev. B* **2019**, *100*, 045413.
- (33) Bose, S.; Ayyub, P. A review of finite size effects in quasi-zero dimensional superconductors. *Rep. Prog. Phys.* **2014**, *77*, 116503.
- (34) Yuan, Y.; Wang, X.; Song, C.; Wang, L.; He, K.; Ma, X.; Yao, H.; Li, W.; Xue, Q.-K. Observation of Coulomb Gap and Enhanced Superconducting Gap in Nano-Sized Pb Islands Grown on SrTiO₃. *Chin. Phys. Lett.* **2020**, *37*, 017402.
- (35) de la Barrera, S. C.; Sinko, M. R.; Gopalan, D. P.; Sivadas, N.; Seyler, K. L.; Watanabe, K.; Taniguchi, T.; Tsien, A. W.; Xu, X.; Xiao, D.; Hunt, B. M. Tuning Ising superconductivity with layer and spin–orbit coupling in two-dimensional transition-metal dichalcogenides. *Nat. Commun.* **2018**, *9*, 1427.
- (36) Von Delft, J.; Ralph, D. C. Spectroscopy of discrete energy levels in ultrasmall metallic grains. *Phys. Rep.* **2001**, *345*, 61–173.

- (37) Schneider, W.-D. Coulomb blockade phenomena observed in supported metallic nanoislands. *Front. Phys.* **2013**, *1*, 13.
- (38) Lafarge, P.; Joyez, P.; Esteve, D.; Urbina, C.; Devoret, M. Measurement of the even-odd free-energy difference of an isolated superconductor. *Phys. Rev. Lett.* **1993**, *70*, 994.
- (39) Brun, C.; Müller, K. H.; Hong, I.-P.; Patthey, F.; Flindt, C.; Schneider, W.-D. Dynamical Coulomb blockade observed in nanosized electrical contacts. *Phys. Rev. Lett.* **2012**, *108*, 126802.
- (40) Vlaic, S.; Pons, S.; Zhang, T.; Assouline, A.; Zimmers, A.; David, C.; Rodary, G.; Girard, J.-C.; Roditchev, D.; Aubin, H. Superconducting parity effect across the Anderson limit. *Nat. Commun.* **2017**, *8*, 1–8.
- (41) Stepanov, P.; Das, I.; Lu, X.; Fahimniya, A.; Watanabe, K.; Taniguchi, T.; Koppens, F. H. L.; Lischner, J.; Levitov, L.; Efetov, D. K. Untying the insulating and superconducting orders in magic-angle graphene. *Nature* **2020**, *583*, 375–378.
- (42) Wan, W.; Dreher, P.; Muñoz-Segovia, D.; Harsh, R.; Guinea, F.; de Juan, F.; Ugeda, M. M. Observation of superconducting Leggett modes from competing pairing instabilities in single-layer NbSe₂. **2021**, arXiv:2101.04050. ArXiv. <https://arxiv.org/abs/2101.04050> (accessed November 23, 2021).
- (43) Hamill, A.; Heischmidt, B.; Sohn, E.; Shaffer, D.; Tsai, K.-T.; Zhang, X.; Xi, X.; Suslov, A.; Berger, H.; Forró, L.; Burnell, F. J.; Shan, J.; Mak, K. F.; Fernandes, R. M.; Wang, K.; Pribiag, V. S. Two-fold symmetric superconductivity in few-layer NbSe₂. *Nat. Phys.* **2021**, *17*, 949–954.
- (44) Zhang, J.; Jia, S.; Kholmanov, I.; Dong, L.; Er, D.; Chen, W.; Guo, H.; Jin, Z.; Shenoy, V. B.; Shi, L.; Lou, J. Janus Monolayer Transition-Metal Dichalcogenides. *ACS Nano* **2017**, *11*, 8192–8198.

- (45) Shimazaki, Y.; Schwartz, I.; Watanabe, K.; Taniguchi, T.; Kroner, M.; Imamoğlu, A.
Strongly correlated electrons and hybrid excitons in a moiré heterostructure. *Nature*
2020, *580*, 472–477.

Supporting Information:

Confinement-engineered superconductor to correlated-insulator transition in a van der Waals monolayer

Somesh Chandra Ganguli,^{*} Viliam Vaňo, Shawulienū Kezilebieke, Jose L. Lado,^{*}
and Peter Liljeroth^{*}

Department of Applied Physics, Aalto University, FI-00076 Aalto, Finland

E-mail: somesh.ganguli@aalto.fi; jose.lado@aalto.fi; peter.liljeroth@aalto.fi

Methods

MBE growth. Sub-monolayer NbSe₂ was grown by molecular beam epitaxy (MBE) on highly oriented pyrolytic graphite (HOPG) under ultra-high vacuum conditions (UHV, base pressure $\sim 1 \times 10^{-10}$ mbar). HOPG crystal was cleaved and subsequently out-gassed at $\sim 400^\circ\text{C}$. High-purity Nb and Se were evaporated from an electron-beam evaporator and a dual-filament low temperature Knudsen cell, respectively. The flux ratio of Nb to Se was controlled to be $\sim 1 : 30$. During the growth the substrate temperature was kept at $\sim 330^\circ\text{C}$, and after the growth the sample was annealed at the same temperature for 1 hour. The growth speed was determined by checking the coverage of the as-grown samples by scanning tunneling microscopy (STM). For higher temperature growth ($> 500^\circ\text{C}$), we obtain significant proportion of 1T-NbSe₂ islands.

STM/STS measurements. Subsequent to the growth, the sample was transferred to a low-temperature STM (Unisoku USM-1300) housed in the same UHV system. STM imaging and STS experiments were performed at $T = 350$ mK. STM imaging was performed in constant current mode. Differential conductance (dI/dV) spectra were measured using standard lock-in techniques sweeping the sample bias in an open feedback loop with rms bias modulation of $70 \mu\text{V}$ at a frequency of 873.7 Hz.

Determination of the island size. The size of the islands were determined using WSxM software,^{S1} where the area of the feature size having height $\sim 6 \text{ \AA}$ (monolayer height) was used as the area of a monolayer island (Fig. S1). Lateral size was determined as $\sqrt{\text{area}}$.

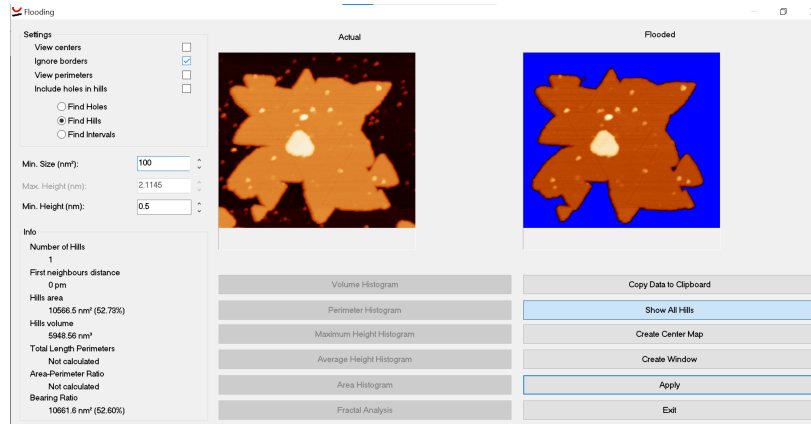


Figure S1: Determination of monolayer NbSe_2 island size using WSxM software.

Determination of the SC and Coulomb gap magnitudes. For determining the average SC gap, spectra were averaged over a $12.5 \times 12.5 \text{ nm}^2$ area 10 nm away from the edge of the island. The data in Fig. 2 was recorded on islands that were non-proximitized (i.e. had no other islands in their immediate vicinity).

At first, the dI/dV spectra on the superconducting islands were normalized with respect to the normal state conductance. These normalized dI/dV spectra had a temperature independent V-shaped background at above superconducting T_c which was also apparent in the lowest temperature (at 350 mK) spectra as shown in Fig. S2(a). This is the well known Altshuler-Aronov effect due to electronic interactions. So, this background was subtracted

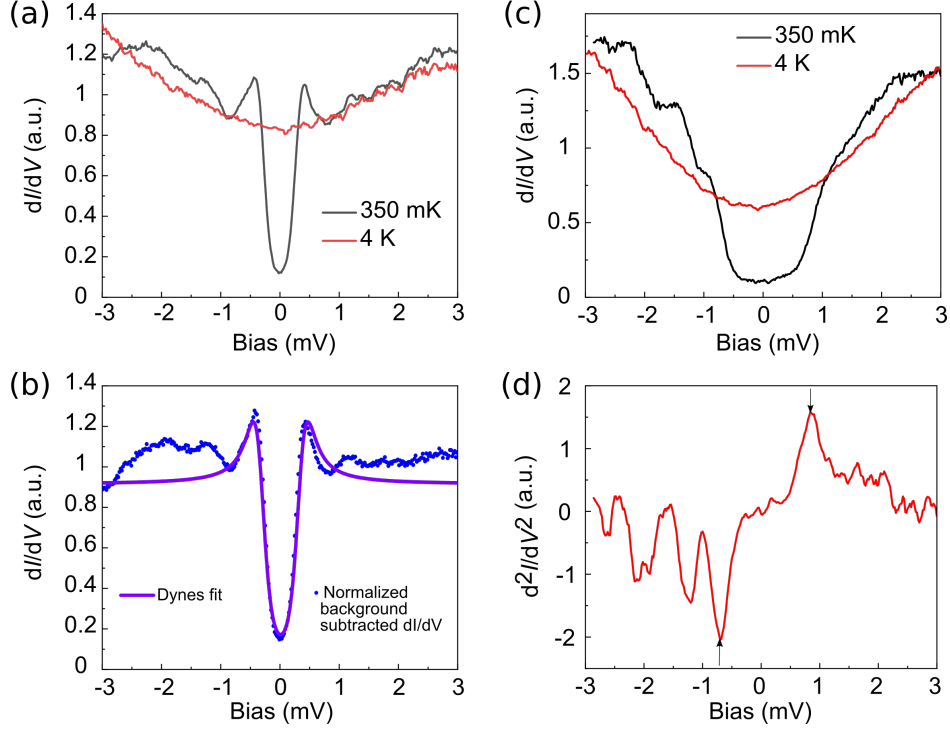


Figure S2: Background removal and fit of SC spectra and estimation of Coulomb gap: (a) Normalized 350 mK and 4 K spectra, taken in 18400 nm² island. (b) 350 mK spectrum after removing the 4 K background along with its Dynes fit. (c) Coulomb gap spectra taken in 329 nm² island (spectrum at $T = 4$ K shown for reference. (d) Numerical derivative d^2I/dV^2 of the 350 mK spectrum (arrows indicate Coulomb gap energies).

by dividing the superconducting spectra with the 4K spectra and the resultant spectra was fitted to the Dynes function $N_S(E) = \Re\left(\frac{|E| + i\Gamma(T)}{\sqrt{(|E| + i\Gamma(T))^2 - \Delta(T)^2}}\right)$ as shown in Fig. S2(b). Here, $N_S(E)$ denotes the normalized background subtracted SC density of states, \Re denotes the real part, $\Gamma(T)$ is the temperature dependent quasiparticle lifetime broadening parameter, also known as the Dynes parameter and $\Delta(T)$ is the temperature dependent SC energy gap. The size dependence of the extracted Dynes parameter is shown in Fig. S3.

To extract the Coulomb gap magnitude the raw spectra (Fig. S2(c)) was numerically differentiated to obtain d^2I/dV^2 , which has a characteristic peak-dip features in positive and negative biases respectively, as shown by arrows in Fig. S2(d). The average bias voltage location for peak and dip was taken to be the Coulomb gap.

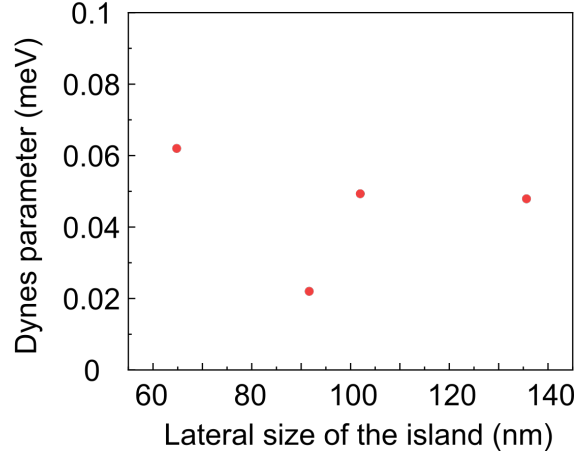


Figure S3: Size dependence of Dynes parameter from the fit with respect to the size of the SC islands.

Size dependence of CDW and band structure

In Fig. S4(a,c,e), we show the presence of 3×3 charge density wave in islands of sizes 480 nm^2 , 1130 nm^2 and 9500 nm^2 respectively as indicated by their respective fast Fourier transforms (FFT) in Fig. S4(b,d,f). This indicates that the 3×3 CDW modulation present in the extended monolayer NbSe₂ survives down to the length scales where correlations are observed. Also, the intensity of the CDW modulation becomes inhomogeneous in the correlated regime. This is a further signature of the strengthening of interactions; perhaps such a change could be associated to an additional charge ordering promoted by interactions. In Fig. S4(g), the large bias dI/dV remains unchanged with island sizes showing the characteristic Nb d-band feature observed in the extended monolayer. All these results clearly demonstrates that the 2H-polytype of NbSe₂ survives down to the length scales where correlations are being observed.

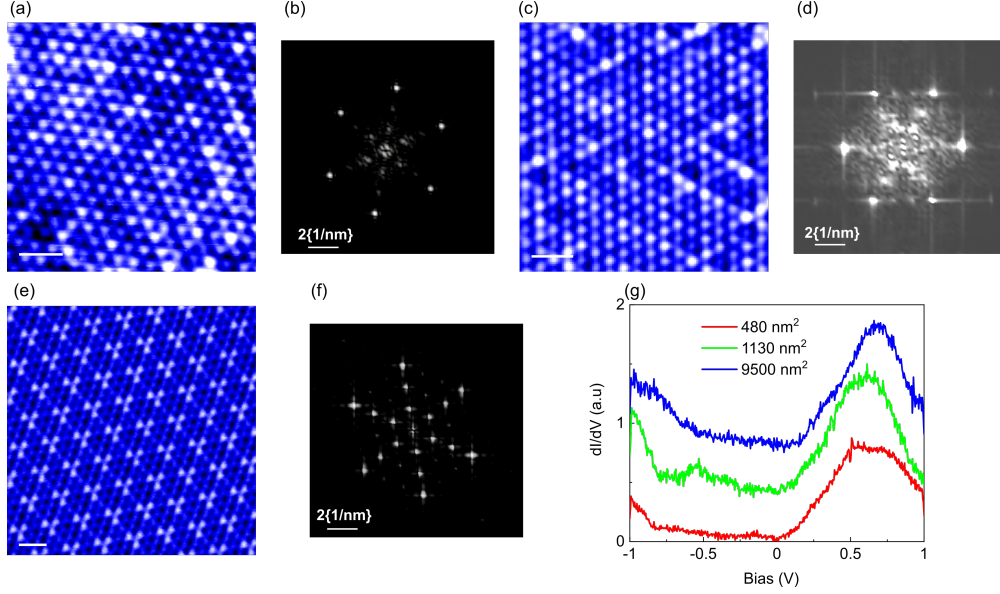


Figure S4: Size dependence of CDW and band structure. Examples of STM images and the corresponding FFTs showing the presence of the CDW state for NbSe₂ islands of different sizes: (a),(b) Island size 480 nm², (c),(d) Island size 1130 nm², (e),(f) Island size 9500 nm². Scale bars 1 nm. (g) Large bias range dI/dV spectra showing the presence of the Nb d-band at the Fermi level for all island sizes.

Magnetic field dependence

In Figure S5, we characterise and distinguish the different types of observed spectra by their respective magnetic field dependencies. The representative spectra chosen are superconducting (SC) spectra from island of size 4200 nm² (Fig. S5(a)), Coulomb gapped spectra from island of size 650 nm² (Fig. S5(b)), and proximitized SC spectra from island of size 650 nm² (Fig. S5(c)). The Coulomb nature of the island having size 2700 nm² becomes evident from the dI/dV taken at magnetic field of 3 T, which is greater than H_{c2} for the superconducting islands. As shown in Fig. S5(d), the superconducting island having size close to the SC-Coulomb phase boundary (4200 nm²) and larger SC island (8400 nm²) have almost indistinguishable dI/dV at $H = 3$ T whereas in the 2700 nm² island, significantly prominent gap signature is present easily distinguishable from the larger SC islands. The fitted BCS gap magnitude for island of size 4200 nm² decreases monotonically to zero with increasing field, whereas Coulomb gap in 650 nm² island remains finite and almost constant

(Fig. S5(e)). The normalized zero bias conductance (ZBC) of both SC and proximitized SC spectra monotonically increases to one with increasing field whereas ZBC for Coulomb gap remains almost constant with increasing field (Fig. S5(f)).

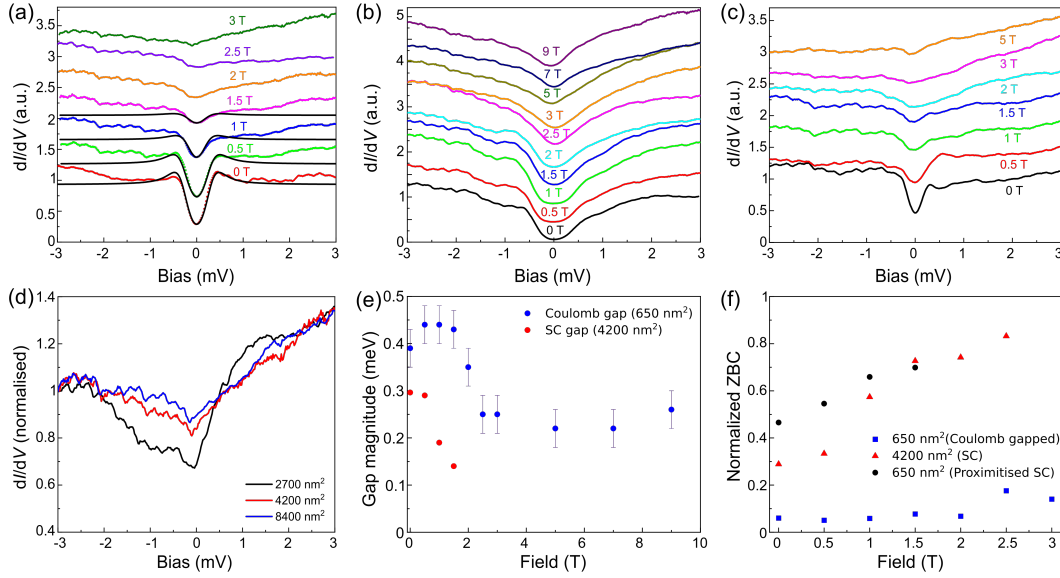


Figure S5: Magnetic field dependence of SC gap, Coulomb gap and proximitised SC gap. Magnetic field dependence of dI/dV spectra in island of size (a) 4200 nm² including BCS fits up to 1.5 T, (b) 650 nm², (c) 650 nm² having proximity to SC island. (d) Comparison of dI/dV taken at 3 T on islands with sizes of 2700, 4200 and 8400 nm². (e), (f) Magnetic field dependence of (e) gap magnitude and (f) normalized zero bias conductance. Spectra in panels (a),(b),(c) are offset vertically for clarity.

It is worthwhile to note that even for large SC islands we still have a small residual gap at high magnetic fields which could be attributed to a correlated pseudogap state that appears when the superconductivity is quenched, and can have additional symmetry broken states of charge or spin-ordering. Precise nature of this pseudogap state remains an open question in the field of correlated superconductors. It is noted that the small residual gap in high fields observed in Pb islands was attributed to the Coulomb gap.^{S2}

Spatial dependence of point spectra within a single island

In Fig. S6(a,b), we demonstrate the representative spectra in edge and middle of a Coulomb-gapped island indicating that the magnitude of the Coulomb gap remains constant. Spatial variation of SC spectra is demonstrated in Fig. S6(d,g) for 2 different sized islands in Fig. S6(c,f) having areas 10400 nm^2 and 18400 nm^2 , respectively (lateral sizes 102 nm and 136 nm, respectively). It is observed that the edges of the SC islands shows larger SC gap compared to the middle of the islands and this variation is larger for bigger islands. In fig. S6(e), the linespectra across CDW domain wall in fig. S6(c) (shown in red dotted line), indicates unchanged SC gap. Fig. S6(h) shows the spatial variation of the fitted SC gap with Dynes equation for spectra taken in island in Fig. S6(e). Fig. S6(i) shows spatial asymmetry: $(dI/dV(V = V_{cp}) - dI/dV(V = -V_{cp}))$, where V_{cp} is the bias corresponding to the coherence peak positions).

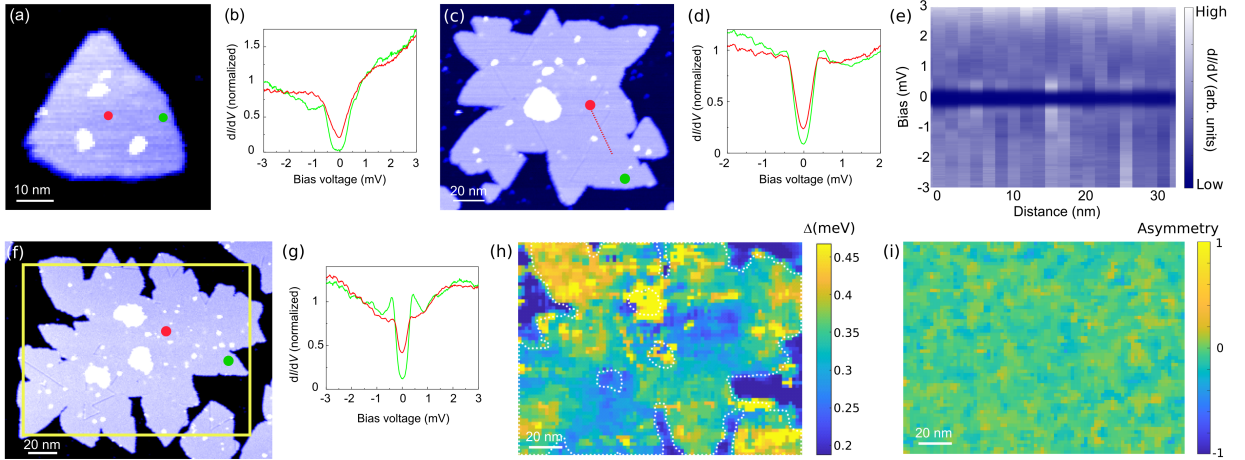


Figure S6: Spatial variation of dI/dV on island sizes. (a) Island size 650 nm^2 . (b) Point spectra taken at indicated locations in (a). (c) Island size 10400 nm^2 . (d) Point spectra taken at indicated locations in (c). (e) Line spectra across the domain wall indicated by the red dotted line in (c). (f) Island size 18400 nm^2 . (g) Point spectra taken at indicated locations in (f). (h) Superconducting gap map from the Dynes fit of the dI/dV map taken at the area indicated by yellow rectangle at (f). The outline of the island's topographic feature is indicated by white dashed line. (i) Spatial asymmetry map.

Superconducting gap map and zero bias conductance map of smallest superconducting island

For the smallest island on which the superconducting spectra was observed (size $\sim 4200 \text{ nm}^2$), dI/dV map was obtained over an area $12.5 \text{ nm} \times 12.5 \text{ nm}$ (Fig. S7(a)). The gap obtained from the fitted spectra with Dynes model and the normalised zero bias conductance shows spatial variation as seen in Fig. S7(b,c). It is also apparent from the spatial variations that the regions where ZBC is higher, SC gap is lower and vice versa. ZBC vs SC gap plot fit gives a slope of ~ -0.54 indicating strong anticorrelation.

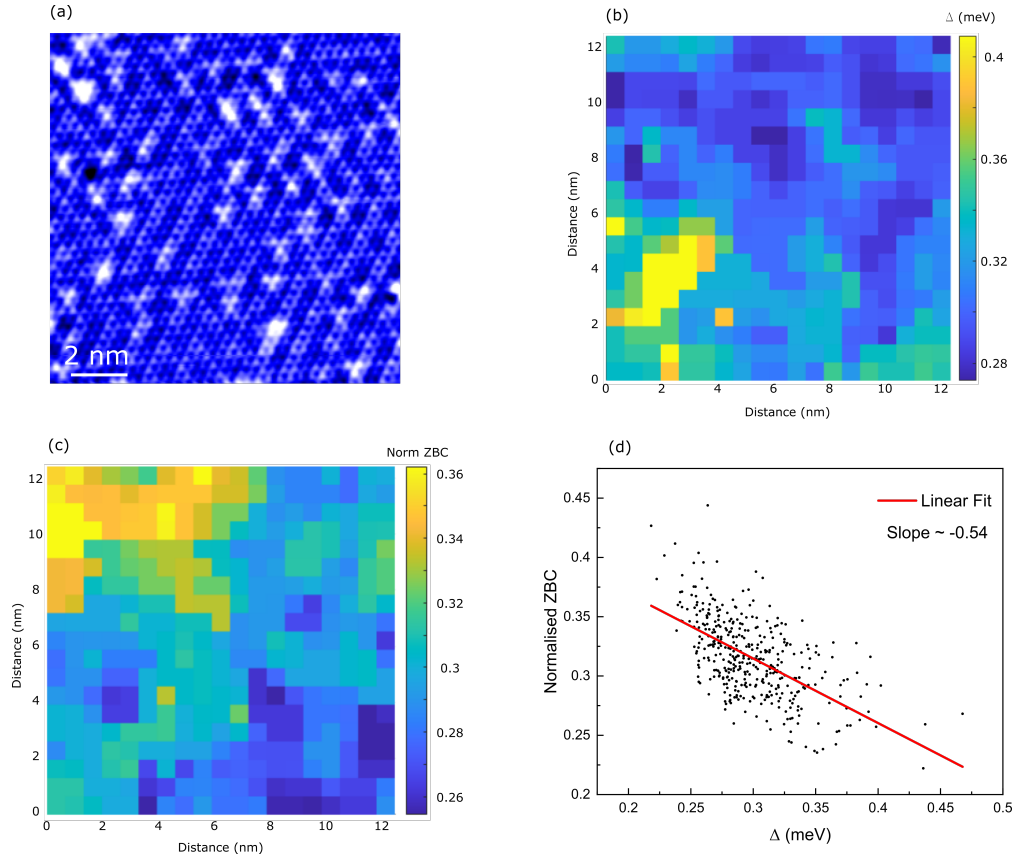


Figure S7: Spatial variation of superconducting gap and ZBC in superconducting island of size 4200 nm^2 . (a) Atomic resolution of the area. (b) Spatial variation of fitted SC gap. (c) Spatial variation of ZBC. (d) ZBC vs SC gap along with its linear fit yields a slope of -0.54 .

Dependence of the transition on the number of many-body orbitals

Here we show that the transition between the correlated gap and the superconducting gap takes place independently on the number of orbitals considered in the calculation. In particular, we show in Fig. S8 the spectral function as a function of the size of the island, taking a different number of many-body orbitals in the calculations. It can be clearly seen that both for $2n = 10$ (Fig. S8(a)) and $2n = 12$ (Fig. S8(b)) orbitals, a transition between a correlated gap to a superconducting one emerges, analogous to the calculations of Fig. 3(a) in the main manuscript. In the absence of U or V there would not be a phase transition between the correlated and superconducting regimes. Nevertheless, in the absence of repulsive interactions, there could still be a phase transition as function of the system size between a single-particle gap coming from quantized energy levels and a superconducting gap. This transition would have an associated smooth evolution of the gap, in contrast with the sharp transition we observe in our data. We finally note that the zero-bias anomaly can be modelled with the model of the dynamical Coulomb blockade.^{S3} While modelling the dynamical Coulomb blockade in this system could be very interesting, it is significantly beyond the scope of this manuscript.

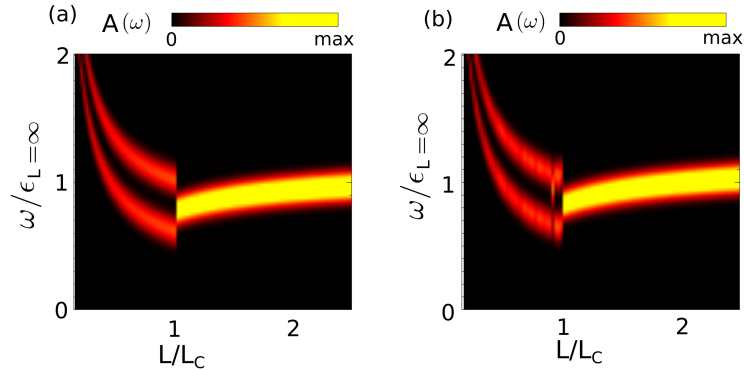


Figure S8: Electronic spectral function as a function of the size of the island, for a different number of many-body orbitals, $2n = 10$ in (a) and $2n = 12$ in (b). It is observed that the transition between different gaps happens irrespective of the number of orbitals.

SC-Coulomb phase boundary as a function of the strength of the proximity effect

Here we address the dependence of the transition between the correlated and superconducting state driven by proximity. First, it is worth noting that in the absence of superconducting proximity, the NbSe₂ would not show the presence of superconductivity due to its finite nature. However, for intermediate islands, the existence of a small proximity drives the system to the superconducting state. The critical length at which such transition takes place depends on the strength of the proximity effect as shown in Fig. S9. The transition remains sharp for finite proximity effects, illustrating that a sharp transition with system size is expected irrespective of the exact value of the superconducting proximity effect.

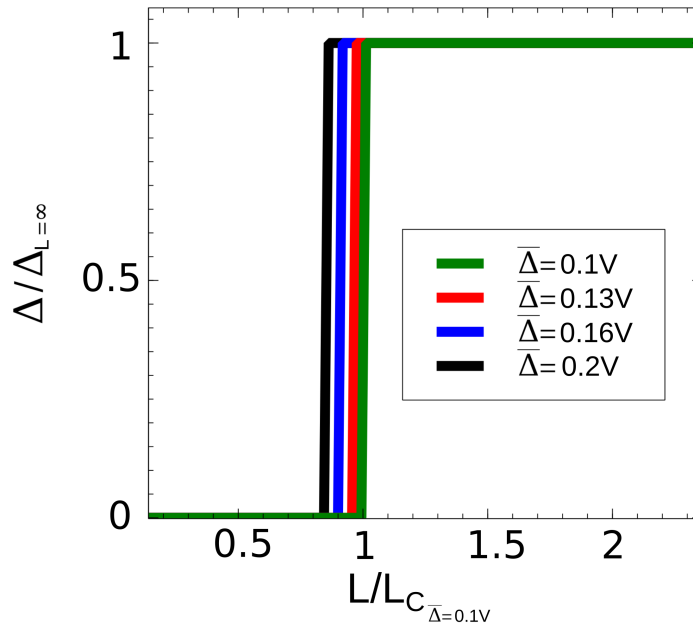


Figure S9: Transition from a correlated gap to a superconducting gap as a function of the size of the island for increasing values of the superconducting proximity effect.

Coulomb-enhanced interactions including charge-density wave and spin-orbit coupling

NbSe₂ is well known for having a complex electronic structure combining Ising spin-orbit coupling and charge density wave. In that regard, it is worth considering whether those effects would have a non-trivial interplay with the confinement enhanced interaction. In this section, we address this issue, showing that Ising spin-orbit coupling nor charge density wave qualitatively change the picture presented in the main manuscript.

In the following we will consider an atomistic tight binding model for the Wannier states of the NbSe₂ band, one per Nb atom, sitting in a triangular lattice.^{S4} The total Hamiltonian takes the form

$$H = H_{\text{kin}} + H_{\text{CDW}} + H_{\text{SOC}} \quad (1)$$

where H_{kin} is the spin-independent hopping term

$$H_{\text{kin}} = \sum_{i,j,s} t_{ij} c_{i,s}^\dagger c_{j,s} \quad (2)$$

H_{CDW} is the charge density-wave order

$$H_{\text{CDW}} = \sum_{i,s} \epsilon_{\text{CDW},i} c_{i,s}^\dagger c_{i,s} \quad (3)$$

and H_{SOC} is the intrinsic Ising spin-orbit coupling

$$H_{\text{SOC}} = i\lambda_{\text{SOC}} \sum_{\langle ij \rangle, s, s'} \gamma_{ij} \sigma_z^{s,s'} c_{i,s}^\dagger c_{j,s'} \quad (4)$$

In the previous terms, t_{ij} is the hopping term that incorporates up to 4th-neighbor hopping, $\epsilon_{\text{CDW},i}$ are the modulated onsite energies associated to the CDW order, $\nu_{ij} = \pm 1$ alternate signs between the different bonds leading to a C_3 symmetric hopping,^{S5} and σ_z is

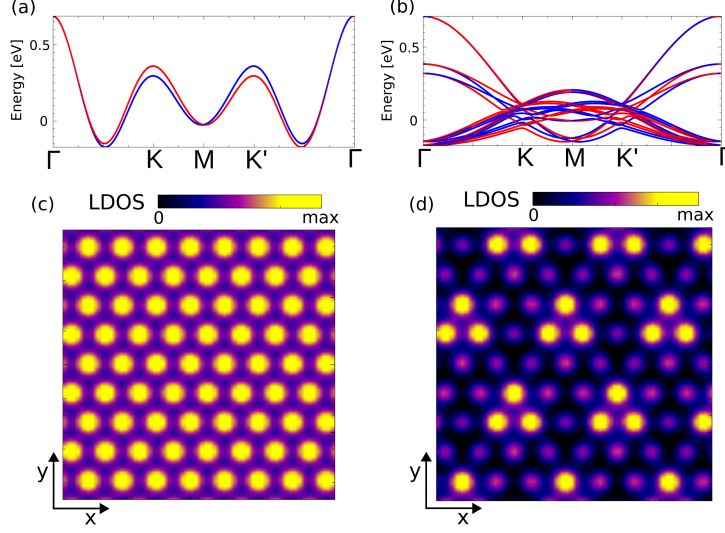


Figure S10: Electronic structure of NbSe₂. Band structure for the minimal unit cell in the absence of CDW (a), and LDOS (c). Panel (b) shows the band structure in the presence of CDW for a 3x3 supercell, and panel (d) shows the LDOS reflecting the spatial charge modulation of the CDW.

the spin Pauli matrix. The band structure and local density of states at Fermi energy are shown in Fig. S10. It is observed that the bands feature the momentum dependent spin-splitting associated to the Ising spin-orbit coupling, and that in the presence of the CDW perturbation the local density of states (LDOS) reproduces the experimentally observed features. As a result, the previous model captures all the microscopic features of NbSe₂.

With the previous Hamiltonian, we now consider the effect of interactions on a finite island. We include interactions in the form of long-range Coulomb interaction in the atomistic model as

$$H_{\text{Coulomb}} = \sum_{i \neq j, s, s'} \frac{V_0}{|\mathbf{r}_i - \mathbf{r}_j|} c_{i,s}^\dagger c_{i,s} c_{j,s'}^\dagger c_{j,s'} \quad (5)$$

where \mathbf{r}_i is the location of Nb atom i , and V_0 is the Coulomb prefactor in atomic units. As this term turns the system into a full-fledge many-body problem, we will consider the impact of interactions only in the lowest energy states. We project this Coulomb interaction to the states closest to the Fermi surface Ψ_α , giving rise to an interaction of the form

$$\mathcal{H}_{\text{Coulomb}} = \sum_{ijkl} \mathcal{V}_{ijkl} \Psi_i^\dagger \Psi_j \Psi_k^\dagger \Psi_l \quad (6)$$

where \mathcal{V}_{ijkl} are obtained by projecting Eq. 5 into the low energy states Ψ_α . We now take finite-size islands with different shapes and different number of atoms, and compute the effective interaction \mathcal{V}_{ijkl} . We perform this procedure on islands whose atomistic Hamiltonian has zero and non-zero spin-orbit coupling and zero and non-zero charge density wave, the results are shown in Fig. S11. As the effective interaction \mathcal{V}_{ijkl} is a four dimensional tensor, generically complex-valued, we will characterize the strength of the repulsive interactions by the average of its absolute value. As shown in Fig. S11, we observe a robust $1/L$ behavior of the projected interaction, independently on the presence or absence of Ising spin-orbit coupling and charge density wave. These results demonstrate that not Ising spin-orbit cou-

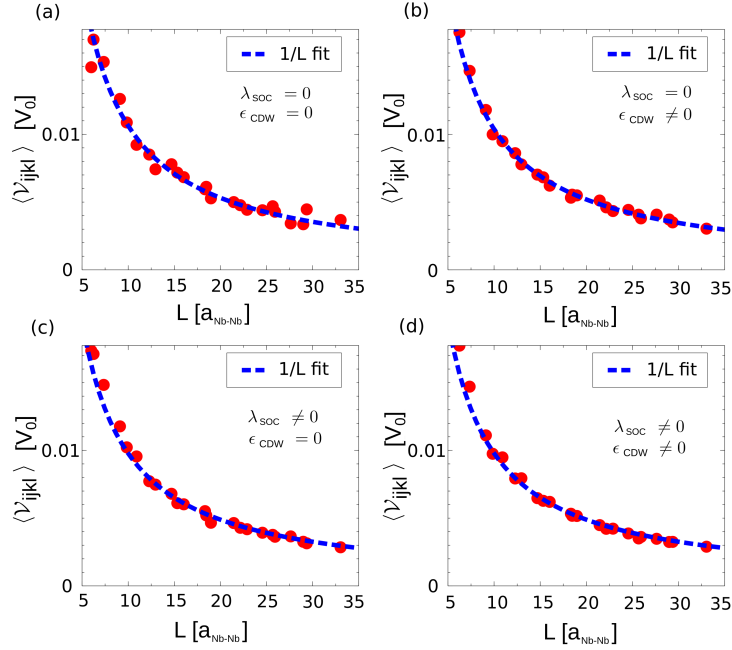


Figure S11: Confinement controlled Coulomb interactions. Average value of the projected interaction \mathcal{V}_{ijkl} on the Fermi surface states Ψ_α . The projected interaction is computed for model zero SOC and zero CDW (a), zero SOC and finite CDW (b), zero CDW and finite SOC (c), and finite CDW and finite SOC (d). It is observed that the average repulsive interaction shows a $1/L$ dependence, with L the size of the island, in agreement with the model in the main manuscript.

pling nor the charge density wave create an impact on the projected interactions and that the repulsive interactions are purely dominated by the island confinement effect.

We now comment on the possibility of extracting the exact parameters for our theoretical model from the experimental data. Extracting U_0 and c_0 and the full dependence of L_C on U_0 , c_0 , V , μ , and $\bar{\Delta}$ would require a very large number of islands so that a detailed error analysis can be done when performing the fitting. Otherwise, small fluctuations would give rise to an inaccurate estimate of U_0 and c_0 . Since at the current stage, our experiments do not allow for a precise estimate of those values, our discussion is focused on highlighting the qualitative behavior of the system rather than providing a specific quantitative extraction of the parameters. From the materials point of view, it is worth noting that U and V are effective interactions projected onto the low energy states, that have a highly non-trivial dependence on the different material parameters of NbSe₂. Furthermore, details such as surface effects and substrate effects could impact these parameters.

Finally, we comment on interaction screening effects in NbSe₂. From the theoretical point of view, providing an accurate estimate of the screening would require performing RPA (random phase approximation) density functional theory (DFT) calculations of the dielectric screening, which would account for both intraband and interband screening in the system. We note that such estimate cannot be reliably performed with the low energy tight binding model we are considering, as interband contributions would be completely neglected in that scenario.

Estimation of coherence length

To estimate the superconducting coherence length, we first fitted the proximitized spectra of Fig. 4 (c) with Dynes' model. The extracted gap values as function of distance was then plotted with an exponential decay to extract the Coherence length in Fig. S12(a). The fitting formula was $\Delta(x) = \Delta_1 - \Delta_2(1 - e^{\frac{-(x-x_0)}{\xi}})$, where $\Delta(x)$, Δ_1 , $(\Delta_1 - \Delta_2)$, x_0 , ξ are fitted gap, SC gap inside the NbSe₂ island, residual SC gap in HOPG (due to proximity of nearby islands), spatial location of the boundary between NbSe₂ and HOPG and the Coherence length respectively. This fit gives us a Coherence length $\xi \approx 7.3$ nm.

Alternatively, the coherence can be determined from the field dependence of the SC island shown in Fig. S12(b). The SC island size here is 8400 nm². From the linear interpolation of the normalized zero bias conductance (ZBC), we can estimate the upper critical field (H_{C2}), which comes out to be ≈ 2.47 T. So, the estimated coherence length will be $\xi = \sqrt{\frac{1}{2\pi} \frac{\phi_0}{H_{c2}}} = 11.5$ nm.

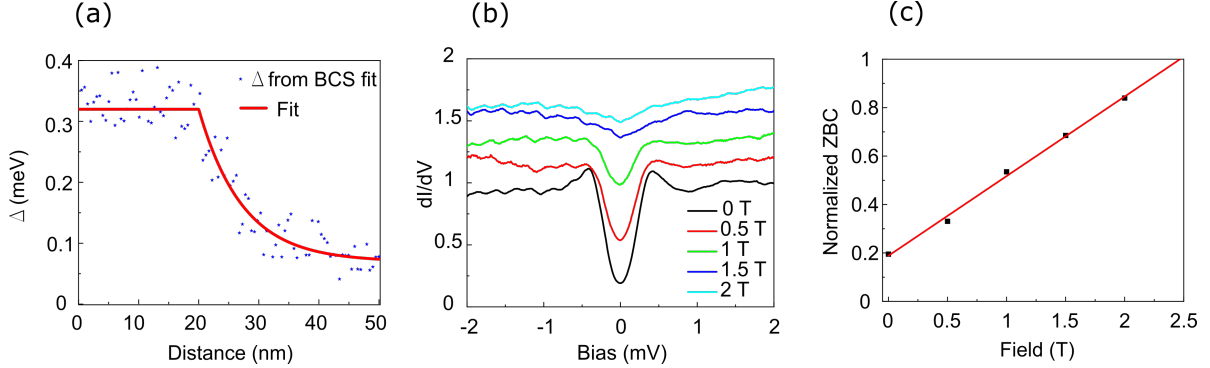


Figure S12: Estimation of Coherence length. (a) Exponential fit of proximitised SC gap. (b) Magnetic field dependence of SC spectra. (c) Linear interpolation of normalized ZBC.

Spatial dependence of islands in proximity

The proximity induced SC gap in the island in Fig. S13(a) varies spatially as illustrated in Fig. S13(b). We observe the presence of SC order by the dip in the conductance at zero bias and the presence of coherence peaks in the different locations of the proximitised island. It indicates that the SC order has been established in the entire island. The SC spectra is asymmetric in conductance values at the coherence peak locations. There is however a variation in the asymmetry observed in the individual spectra at different locations. The histogram of the asymmetry defined by the (normalised conductance at -ve coherence peak location)-(normalised conductance at +ve coherence peak location) shows a distribution asymmetric about zero (mean value of 0.11 from Gaussian fit). The proximitised non-SC island in Fig. S13(d) have variations in the local spectra as seen from Fig. S13(e). Here, the strong electron-hole asymmetries are typical of a non-superconducting origin of the gap,^{S6} and support the strongly correlated nature of the small islands.

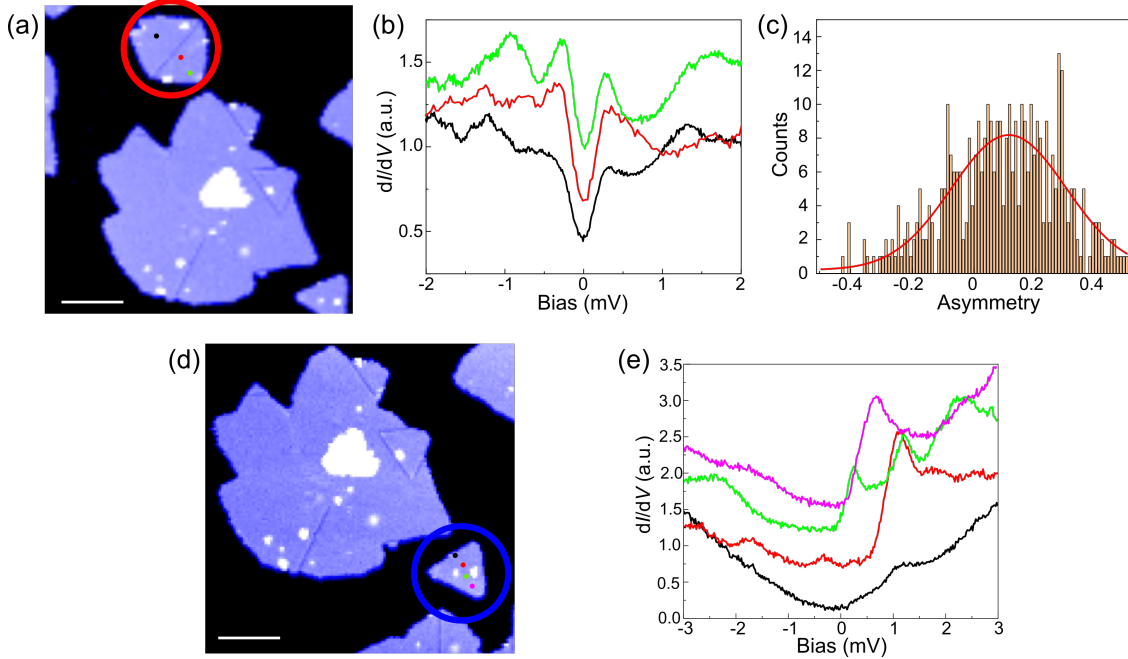


Figure S13: Spatial variation of proximitised spectra. (a) Proximitised superconducting island. Scale bar, 20 nm. (b) Point spectra at the indicated locations. (c) Statistical distribution of the asymmetry in the individual spectra and its Gaussian fit. (d) Proximitised non-superconducting island. Scale bar, 20 nm. (e) Point spectra at the indicated locations.

References

- (S1) Horcas, I.; Fernández, R.; Gomez-Rodriguez, J.; Colchero, J.; Gómez-Herrero, J.; Baro, A. WSXM: a software for scanning probe microscopy and a tool for nanotechnology. *Rev. Sci. Instrum.* **2007**, *78*, 013705.
- (S2) Yuan, Y.; Wang, X.; Song, C.; Wang, L.; He, K.; Ma, X.; Yao, H.; Li, W.; Xue, Q.-K. Observation of Coulomb Gap and Enhanced Superconducting Gap in Nano-Sized Pb Islands Grown on SrTiO₃. *Chin. Phys. Lett.* **2020**, *37*, 017402.
- (S3) Ingold, G.-L.; Nazarov, Y. V. In *Single Charge Tunneling: Coulomb Blockade Phenomena In Nanostructures*; Grabert, H., Devoret, M. H., Eds.; Springer: Boston, 1992; pp 21–107.
- (S4) Smith, N. V.; Kevan, S. D.; DiSalvo, F. J. Band structures of the layer compounds 1T-TaS₂ and 2H-TaSe₂ in the presence of commensurate charge-density waves. *J. Phys. C Solid State Phys.* **1985**, *18*, 3175–3189.
- (S5) Kane, C. L.; Mele, E. J. Quantum spin Hall effect in graphene. *Phys. Rev. Lett.* **2005**, *95*, 226801.
- (S6) Cai, P.; Ruan, W.; Peng, Y.; Ye, C.; Li, X.; Hao, Z.; Zhou, X.; Lee, D.-H.; Wang, Y. Visualizing the evolution from the Mott insulator to a charge-ordered insulator in lightly doped cuprates. *Nat. Phys.* **2016**, *12*, 1047–1051.